Please do not adjust margins

Journal Name

ARTICLE

MCM-41 support to ultrasmall γ-Fe_2O_3 nanoparticles for H_2S removal†

Received 00th January 20xx,
Accepted 00th January 20xx

DOI: 10.1039/c7ta03652c

www.rsc.org/

C. Cara,[abc] E. Rombi,[a] A.Musinu,[ac] V. Mameli,[ac] A. Ardu,[abc] M. Sanna Angotzi,[ac] L. Atzori,[a] D. Niznansky,[d] H. L. Xin[e] and C. Cannas*[abc]

MCM-41 is proposed to build mesostructured Fe_2O_3-based sorbents as an alternative to other silica or alumina supports for mid-temperature H_2S removal. MCM-41 was synthesized as micrometric (MCM41_M) and nanometric (MCM41_N) particles and impregnated through an efficient Two-Solvents (hexane-water) procedure to obtain the corresponding γ-Fe_2O_3@MCM-41 composites. The active phase is homogeneously dispersed within the 2 nm channels in form of ultrasmall maghemite nanoparticles assuring a high active phase reactivity. The final micrometric (Fe_MCM41_M) and nanometric (Fe_MCM41_N) composites were tested as sorbents for the hydrogen sulphide removal at 300 °C and the results were compared with a reference sorbent (commercial unsupported ZnO) and an analogous silica-based sorbent (Fe_SBA15). MCM-41 based sorbents, having the highest surface areas, showed superior performances that were retained after the first sulphidation cycle. Specifically, the micrometric sorbent (Fe_MCM41_M) showed a higher SRC value than the nanometric one (Fe_MCM41_N), due to the low stability over time of the nanosized particles caused by their high reactivity. Furthermore, the low regeneration temperature (300-350 °C), besides the high removal capacity, render MCM41-based systems an alternative class of regenerable sorbents for thermally efficient cleaning up processes in Integrated Gasification Combined Cycles (IGCC) systems.

Introduction

Sulphur cleaning processes (desulphidation) of gas phase from sulphur compounds, commonly present in syngas, have been receiving dramatic attention since hazardous, corrosive, and toxic gases cause environmental damages and industrial challenges.[1] Commonly, H_2S or other sulphur compounds are removed *via* low-temperature (40-50 °C) amine scrubbers, requiring the cooling and the following re-heating of the syngas.[2] This drawback can be overcome by the use of mid- (300-600 °C) and high-temperature (600-850 °C) syngas cleaning processes.[2,3] In this context, different types of metal oxides have been proposed as potential sorbents in a wide range of temperatures based on thermodynamic calculations.[4] Among them, zinc oxide has a high equilibrium constant for sulphidation leading to a low H_2S concentration but with slow kinetics, which limits its sulphur loading capacity.[1,3,4] Iron oxide, on the other hand, has rapid kinetics, namely a high sulphur loading capacity, but its equilibrium constant is lower than that of zinc oxide.[1,2,5] Solid sorbents made up of non-supported zinc or iron oxides, also in form of nanostructured materials, have been proposed in some pilot plants;[6,7] however their sintering during the successive mid-temperature or high-temperature sorbent cycles induces a dramatic decrease in their performances.[8] In the last decade, due to the potential benefit in terms of overall thermal efficiency of the IGCC (Integrated Gasification Combined Cycles) plant, arising from the use of mid-temperatures for sulphidation and regeneration cleaning processes, the research is moving toward the development of two main categories of sorbents: supported active phases[9–12] and the recently proposed mesoporous active phases.[2,13–16] The dispersion of metal oxide active phases in different types of silica supports improves the gas-solid H_2S-MeO_x interaction and allows their regeneration.[17,18] The surface area can be optimized by changing the pore size and the wall thickness, as well as the mesoporous structure.[19] The recent efforts in the fine tuning of the features of mesostructured siliceous materials have opened the road to the design of highly thermally stable supports for highly efficient and regenerable catalysts[10–12] and sorbents.[18] ZnO-SBA15[17] and Fe_2O_3-SBA15[20] nanocomposites have been found to be highly efficient and regenerable sorbents due to the effective dispersion of the active phase within the mesochannels of the hexagonally ordered porous structure. Therefore, tuning the support features (nature and

a. Department of Chemical and Geological Sciences, University of Cagliari, S.S. 554 bivio per Sestu, 09042, Monserrato (CA), Italy. E-mail: ccannas@unica.it
b. Consorzio AUSI, CREATE, Palazzo Bellavista Monteponi, 09016 Iglesias, CI, Italy
c. INSTM, Cagliari Unit
d. Department of Inorganic Chemistry, Charles University of Prague, Prague 116 36, Czech Republic
e. Center for Functional Nanomaterials, Brookhaven National Laboratory, Upton, New York, United States

† Electronic Supplementary Information (ESI) available: experimental conditions for the synthesis of the composites FTIR, N_2-physisorption, TPD regeneration profile, XRD, H_2S breakthrough curves. See DOI: 10.1039/x0xx00000x

Please do not adjust margins

Please do not adjust margins

textural properties) could in principle represent a further step to the design of sorbents with improved performances.

The present work deals with the use of MCM-41 mesostructured silicas as an alternative to SBA-15 and other conventional silica or alumina supports for the preparation of iron oxide-based sorbents for mid-temperature H_2S removal. The iron oxide phase was chosen because of its low cost, non-toxic[21] and promising desulphidation-regeneration performance at mid-temperature. In this framework, different samples with the same active phase loading (10%w/w) were prepared by an efficient Two-Solvents (hexane/water) impregnation route to understand how the different features of the supports affect the H_2S sorption capacity. The combined use of ^{57}Fe Mössbauer Spectroscopy and DC magnetic measurements was exploited to study the iron oxide phase. In order to study the effect of different pore dimensions, SBA-15 (Ø = 7 nm) and MCM-41 (Ø = 2 nm) composites, both as micrometric particles with hexagonal porous structure, were prepared. Finally, MCM-41-based systems with the same pore dimension (Ø = 2 nm) as micrometric and nanometric particles were synthesized to study the influence of the channels length.

Experimental

Chemicals

All chemicals were of analytical grade and used as received without further purification. Hexadecyltrimethylammonium bromide (CTAB, 98%), Pluronic P123, Ethanol (azeotropic 95.6%), Ethyl acetate (EtOAc, 99.8%), Ammonium hydroxide (NH_4OH, 28% NH_3 in H_2O), Tetraethyl orthosilicate (TEOS, 98%), Iron (III) nitrate-nonahydrate (>99.5%), n-Hexane (95%) were purchased from Sigma-Aldrich. Distilled water was used for all the experiments.

Preparation of Hexagonal mesostructured silica (SBA-15, MCM-41)

SBA-15 was obtained according to the procedure reported by Zhao *et al.*[22] MCM-41 supports with different particles size were prepared by setting up different synthetic approaches, starting from a procedure reported in the literature for micrometric systems.[23] The detailed description of the synthetic routes used to obtain the different MCM-41 supports is reported in the following.

Support preparation

MCM41_M. Micrometric silica particles were synthesized by using 1 g of hexadecyltrimethylammonium bromide (CTAB) in 200 mL of distilled water and keeping the solution under stirring at 300 RPM for 3 hours at room temperature. Then, 87 mL of ethanol and 21 mL of ammonium hydroxide were added; after 20 min, the stirring speed was increased to 600 RPM before adding 3.79 mL of tetraethyl orthosilicate. The starting transparent solution became white opalescent and the resulting dispersion was kept for 19 hours under mild stirring (300 RPM). Finally, the white solid was separated from the solution by centrifugation and washed three times with 20 mL of a 1:1 V/V mixture of ethanol and water. The solid was dried overnight at 80 °C and then calcined at 550 °C for 4 hours (heating rate, 5 °C min^{-1}) to remove the organic template. The complete removal of the surfactant was verified by FTIR analysis (Fig. S1†).

MCM41_N. Nanometric (100-200 nm) silica particles were obtained by using the following procedure: an aqueous solution of CTAB (0.4 g of CTAB in 400 mL of distilled water) was kept under stirring (300 RPM) for 1 hour and 12 mL of ammonium hydroxide and 1 mL of ethyl acetate were subsequently added. After 5 min, the stirring speed was increased to 600 RPM, and 1 mL of TEOS was then added. The resulting opalescent dispersion was kept for 3 hours under mild stirring (300 RPM). Separation, washing, drying and calcination processes were performed as reported for the MCM41_M. The complete removal of the surfactant and of ethyl acetate was verified by FTIR analysis (Fig. S1†).

Sorbents preparation

Mesostructured silica-based Fe_2O_3 composites were prepared *via* a Two-Solvents impregnation route using n-hexane and water as solvents.[20] Typically, 0.1 g of silica (SBA15, MCM41_M, MCM41_N), dried at 120 °C for 48 hours in air, were suspended in 12 mL of n-hexane and kept under stirring at 300 RPM for 2 hours at room temperature, then a suitable amount of the metal precursor aqueous solution ($Fe(NO_3)_3{\cdot}9H_2O$) was added drop-wise. The necessary volume of solution was calculated according to the pore volume determined by N_2-physisorption analysis (Table S1†), as requested for the incipient wetness impregnation methods.[24] After 2 hours, the dispersion was heated at 80 °C in a hot-plate until complete evaporation of the hexane, and then kept in an oven at 80 °C overnight. Finally, the product was calcined at 500 °C (heating 2 °C min^{-1}) for two hours in order to decompose the iron nitrate. The composites are labelled as Fe_support (Fe_SBA15, Fe_MCM41_M, Fe_MCM41_N). The theoretical loading of the active phase corresponds to the actual loading due to the choice of the incipient wetness impregnation route that does not involve any liquid/solid separation and washing steps.

Characterization

Low-angle (2θ = 0.8°–2.5° for SBA-15 and 2θ = 0.9°–6° for MCM-41) and wide-angle (2θ = 10°–70°) X-ray diffraction patterns were recorded on a Seifert instrument with a θ–θ geometry and a Cu Kα anode. The lattice parameter was calculated by the equation

$$a_0 = \frac{2d_{100}}{\sqrt{3}}$$

Textural analyses were carried out on a Micromeritics 2020 system by determining the nitrogen adsorption–desorption isotherms at -196 °C. Prior to analyses, the samples were heated for 24 hours under vacuum to 250 °C (heating rate, 1 °C min^{-1}). The Brunauer–Emmett–Teller (BET) specific surface

This journal is © The Royal Society of Chemistry 20xx

Please do not adjust margins

Please do not adjust margins

area was calculated from the adsorption data in the P/P_0 range 0.05-0.17 for MCM-41 and 0.05-0.3 for SBA-15. The total pore volume was calculated at P/P_0 = 0.99 for MCM41_M, SBA15 and corresponding composites, while at P/P_0 = 0.87 in the case of the nanometric MCM41_N and relative composite, due to the evident interstitial condensation. The mean pore diameter was determined by applying the Barrett–Joyner–Halenda (BJH) model to the isotherm desorption branch. The wall thickness was calculated as the difference between the lattice parameter (a_0) and the pore diameter (D_{pore}).

Dynamic Light Scattering (DLS) measurements were conducted by a Malvern Instrument Zeta Zetasized Ver 7.03, equipped with a He-Ne laser (λ = 663nm, max 5 mW) and operating at a scattering angle of 173°. For the analyses, 2 mg of silica particles were dispersed in 2 mL of water and sonicated for 2 min. The dispersion was then transferred in a plastic cuvette and analysed. The hydrodynamic diameter was estimated only for the nanometric sample (MCM41_N).

Transmission electron microscopy (TEM) images were obtained by means of a JEOL200CX microscope operating at an accelerating voltage of 160 kV and a JEOL JEM 2010 UHR microscope equipped with a Gatan Imaging Filter (GIF). EDS measurements were carried out in STEM mode using a FEI Talos F200X scanning/transmission electron microscope with a field-emission gun operating at 200 kV, equipped with a four-quadrant 0.9-sr energy dispersive X-ray spectrometer. Finely ground samples were dispersed in ethanol and sonicated, the suspensions were then dropped on carbon-coated copper grids. The particles size distribution was determined for the nanometric sample (Fe_MCM41_N) by manual counting, using Adobe Photoshop and considering the nanoparticles as spheres. The mean particle size ($<D_{TEM}>$) and the standard deviation were calculated by fitting the particles size distribution data with a Gaussian function.

FTIR spectra were collected in the range 400-4000 cm^{-1} using a Bruker Equinox 55 spectrophotometer. The samples were analysed after dispersing the powders in KBr pellets.

^{57}Fe Mössbauer spectra were measured for the Fe_SBA15 and Fe_MCM41_M samples in the transmission mode with ^{57}Co diffuse into a Rh matrix as the source, moving with constant acceleration. The spectrometer (Wissel) was calibrated by means of a standard α-Fe foil and the isomer shift was expressed with respect to the standard at room temperature. The fitting of the spectra was performed with the help of the NORMOS program using Lorentzian profiles.

The magnetic properties of the Fe_MCM41_M sample were studied by using a Quantum Design SQUID magnetometer (Hmax = ± 55 kOe). Zero field cooled–field cooled (ZFC-FC) protocols were used to record the magnetization versus temperature curves within 5–300 K under a 25 Oe magnetic field. The ZFC curve was obtained by heating up the sample from 5 K to 300 K under magnetic field after a cooling process under a zero-magnetic field. The FC curve was obtained by cooling the sample from 5 K to 300 K under a 25 Oe magnetic field. The field dependence of the magnetisation at 5 K has also been studied. The magnetisation values have been normalised for the mass of the active phase (emu/g_{act}).

Elemental analysis (CHNS) was carried out with an EA 1108 CHS-O analyzer (Fisons Instruments) by total combustion of the samples in an oxygen and helium mixture.

Desulphidation and regeneration activity evaluation of sorbents

To determine the desulphidation and regeneration activity, 50 mg of composite were placed on a quartz wool bed (50 mg) in a vertical quartz tubular reactor coaxially located in an electrical furnace. Before desulphurization, a pre-treatment at 300 °C for 30 min under helium flow was performed to remove air and water from the sorbent and the reactor. Then, a reactant gas containing 15200 ppm of H_2S in Helium (inlet flow, 20 cm^3 min^{-1}) was fed to the reactor and the H_2S content in the outlet flow during the adsorption test was monitored by a quadrupole mass spectrometer (Thermo Electron Corporation), with a detection limit for H_2S of about 50 ppm. At the same time, H_2O and SO_2 signals were also monitored. When the outlet concentration of H_2S reached 15200 ppm, the measure was stopped and the system was purged in flowing helium (20 cm^3 min^{-1}) for 1 hour. The amount of sulphur retained per unit mass of sorbent was determined when the outlet H_2S concentration attained 100 ppm by the formula:

$$\text{sulphur retention capacity (SRC)} = \frac{(F_s * B_t)}{W}$$

where F_s is the mass flow rate of sulphur (mg of S s^{-1}), B_t is the breakthrough time (s) and W is the sorbent weight (g), referring to the composite. The sulphur retention capacity of the sorbents was obtained as the difference between the B_t value of the composite and the B_t value of the bare support. The error on the SRC values was estimated at 2 mg_S $g^{-1}_{sorbent}$ by carrying out several sulphidation cycles on fresh portions of the commercial sorbent $Katalko_{JM}$ 32-5. The regeneration process was performed on a Thermoquest 1100 TPD/R/O apparatus equipped with a thermal conductivity detector (TCD) and a quadrupole mass spectrometer (QMS) for monitoring SO_2 and O_2 signals. The composite was heated under air flow (20 cm^3 min^{-1}) up to 500 °C (heating rate, 10 °C min^{-1}) and the temperature was kept constant for 3 hours. To identify the samples after different cycles of sulphurization or regeneration processes, a letter (S o R, respectively) and a number (denoting successive cycles) were added in the sample name.

Results

Sorbent characterization

Fig. 1a reports the wide angle XRD patterns of the bare SBA-15 and MCM-41 supports (SBA15, MCM41_M, MCM41_N) and the corresponding Fe_2O_3 micrometric and nanometric composites calcined at 500 °C with 10%w/w of Fe_2O_3 (Fe_SBA15, Fe_MCM41_M, Fe_MCM41_N). Besides the typical broad reflection of the amorphous silica at about 22°, the presence of two broad and weak reflections at about 35° and 62° indicates the formation of a highly-dispersed iron oxide, probably in the form of very small nanoparticles. Maghemite is

Please do not adjust margins

Please do not adjust margins

the most probable phase, showing the most intense reflection at around 36° (PDF card #139-1346).[20]

In order to ascertain the iron oxide crystalline phase, the samples Fe_SBA15 and Fe_MCM41_M have been further studied by room temperature (RT) ^{57}Fe Mössbauer Spectroscopy (Fig. 1b). The spectra show a doublet with an isomer shift of 0.34 ± 0.01 mm s^{-1} for both samples, ascribable to very small maghemite nanoparticles.[25–27] Further information about the particles size and its distribution can be extracted by the FWHM values of the doublet. FWHM has been found equal to 0.49 ± 0.01 mm s^{-1} and 0.74 ± 0.01 mm s^{-1} for Fe_MCM41_M and Fe_SBA15, respectively. This difference can reasonably be ascribed to different maghemite particles size: the higher value for Fe_SBA15 suggests the presence of particles larger than those of the Fe_MCM41 sample according to the bigger pore size. The presence of maghemite instead of hematite as the active phase is consistent with the magnetic behaviour observed for the sample Fe_MCM41_M by magnetic field (*M vs H*) and temperature (*M vs T*) dependences of the magnetisation (Fig. 1c-d). Indeed, the *M vs H* curves at 5 K show the typical ferro/ferrimagnetic behaviour with a hysteresis loop (H_c=1.59 ± 0.08 kOe; M_r=1.7 ± 0.1 emu/g_{act}) and a saturation state reached at about 40 kOe, giving rise to a saturation magnetisation (M_s) of 8 ± 1 emu/g_{act}. These features are ascribable to a ferrimagnetic phase and suggest the presence of the active phase as maghemite nanoparticles. The low M_s value could be justified by the presence of canted spins, as expected for ultrasmall particles.[28,29] The *M vs T* curves show a typical paramagnetic/superparamagnetic behaviour with a ZFC magnetisation staying at about 0 emu/g_{act} and a FC curve diverging from the ZFC one at temperatures higher than 20 K.

All these findings suggest that the active phase in all the composites is made by ultrasmall ferrimagnetic particles of maghemite, in agreement with the Mössbauer data.

Fig. 2 a, d, and g report the low angle XRD patterns of the calcined supports and the corresponding composites.

All samples show three reflections (100), (110), (200) indicating a long-range order related to a hexagonal pore structure (space group *p6mm*). d-spacing (d_{100}) and cell parameters (a_0) have been calculated for each sample and are reported in Table 1. Higher values of the d_{100} and a_0 have been found for SBA15 in comparison with MCM41 suggesting, as expected, larger pore size and thicker wall. The mesostructure is retained in the composites, but a slight shift of the reflections toward higher angles is observed, suggesting a slight shrinkage of the pore structure as a consequence of the presence of the active phase.[20]

Fig. 2 b, e, and h report representative TEM images of the supports (MCM41_M, MCM41_N and SBA15). Micrometric particles are observed for SBA15 (Fig. 2h) and MCM41_M (Fig. 2b) while spheroidal nanometric particles are obtained in the case of MCM41_N (Fig. 2e).

In agreement with low angle XRD results, TEM analysis confirms the presence of an ordered porous structure with pores dimension of about 2 nm and 7 nm for MCM41 and SBA15, respectively. In the case of MCM41_N, an important reduction in the particle size from the micrometer to the nanometer range is observed, caused by the use of ethyl acetate during the synthesis. In the case of the nanometric sample (MCM41_N), the particles size distribution calculated by TEM images and the hydrodynamic particle size distribution determined by DLS measurements have been compared (Fig. 2e, inset). As expected, the particles size obtained by DLS (Average Hydrodynamic size = 147 nm, Dispersity = 25%) is higher than that obtained by TEM (Average Particle size = 110 nm, Dispersity = 25%).

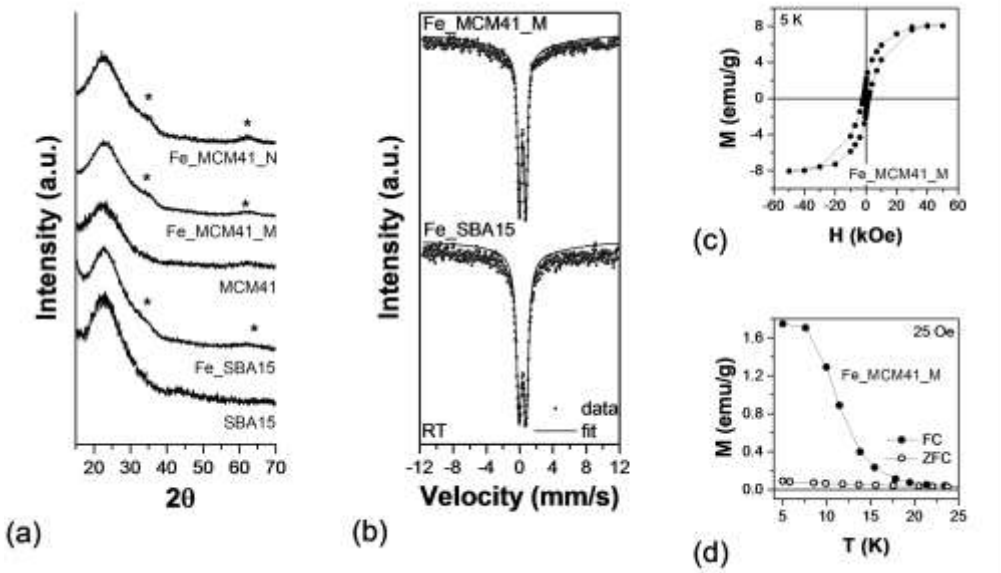

Fig. 1 Wide angle XRD patterns of bare SBA15 and MCM41 and different iron oxide based composites (Fe_SBA15; Fe_MCM41_M and Fe_MCM41_N) (a), ^{57}Fe Mossbauer spectra of Fe_SBA15 and Fe_MCM41_M (b), field dependence (c), and temperature dependence of the magnetisation for the sample Fe_MCM41_M (d).

This journal is © The Royal Society of Chemistry 20xx

Please do not adjust margins

Please do not adjust margins

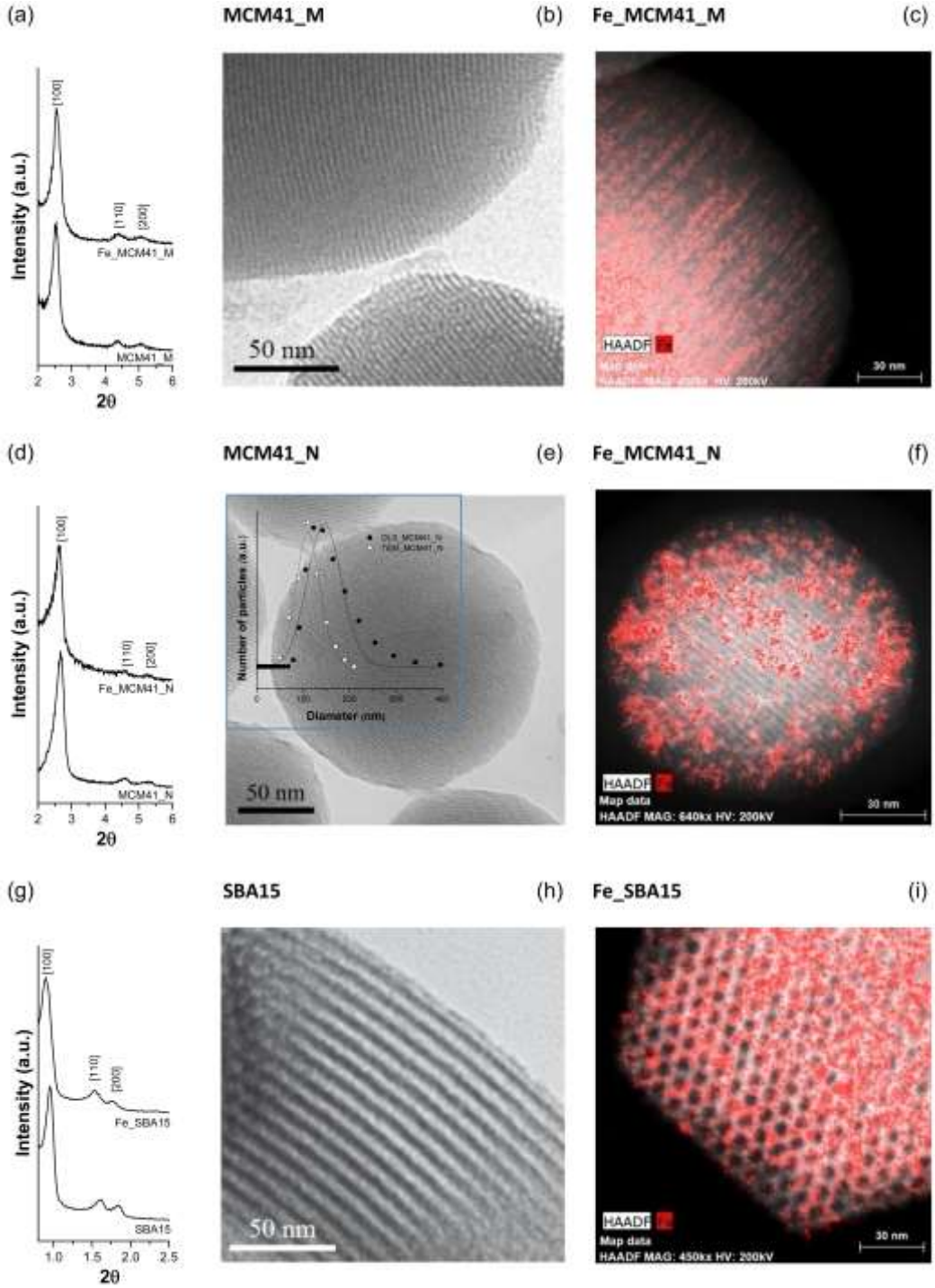

Fig. 2 Low angle of bare supports and corresponding composites (a, d, g) Bright field TEM images of bare SBA15 (b), MCM41_M (e) and MCM41_N (h) at different magnifications. STEM-EDX images of the composites Fe_SBA15 (c), Fe_MCM41_M (f) and Fe_MCM41_N (i). The comparison between the particles size distribution calculated by TEM and the hydrodynamic particle size distribution determined by DLS measurements are also reported for the MCM41_N sample (Fig. 2e, inset).

Please do not adjust margins

Please do not adjust margins

Table 1 Textural features obtained by N_2-physisorption data for the supports and the corresponding composites. S_{BET}=Surface area; V_p=Pore volume; D_p=pore diameter. Relative standard deviation: %RSD(S_{BET})=2.1%; %RSD(V_p)=1.1%; %RSD(D_p)=1.8%. d-spacing (d_{100}) and lattice parameter (a_0) obtained from the X-Ray diffraction data.

Sample	S_{BET} (m^2g^{-1})	V_p (cm^3g^{-1})	D_{pore} (nm)	w_t (nm)	d_{100}	a_0
MCM41_M	1063	0.76	2.3	1.7	3.49	4.0
Fe_MCM41_M	768	0.53	2.2	1.6	3.47	4.0
MCM41_N	1248	0.80	2.2	1.7	3.37	3.9
Fe_MCM41_N	1007	0.58	2.2	1.7	3.33	3.9
SBA15	763	1.10	7.1	4.2	9.29	11.3
Fe_SBA15	601	1.01	6.9	4.5	9.91	11.4

However, by taking into account the different phenomena at the basis of the techniques, the results can be considered in good agreement, being the dispersity equal to 25% in both cases. STEM-EDX mapping of Fe has been also carried out in order to get information about the dispersion of the active phase within the support. Thanks to the recent development of ultrasensitive energy-dispersive X-ray detectors, it has been possible to acquire chemical maps with sub-nanometer spatial resolution.[30,31] The images reported in Fig. 2 c, f, and i show a homogeneous distribution of Fe throughout the support for all the samples, with no evidences for significant iron concentration at the external surface or isolated iron oxide particles. Moreover, it is possible to notice that the iron oxide particles size is very small, lower than the pore diameter, confirming the wide angle XRD and ^{57}Fe Mössbauer data.

Fig. 3 reports the nitrogen adsorption-desorption isotherms and the pore size distributions (PSD) of both the supports and the relative composites. The textural parameters of the different samples are listed in Table 1.

MCM41 supports (MCM41_M and MCM41_N) and the corresponding composites (Fe_MCM41_M and Fe_MCM41_N) exhibit characteristic IVB type behaviour according to IUPAC classification:[32] besides a microporous contribution, the presence of a mesoporous one is clearly indicated by the existence of a well-defined step in the 0.2-0.3 P/P_0 range as a consequence of the capillary condensation. The nanometric systems (MCM41_N and Fe_MCM41_N) show a further condensation step above 0.90 ascribable to interparticles voids, which indirectly reflects the small particle size of these samples.[33] The impregnation process induces, as expected, a reduction in the surface area values (Table 1) mainly due to a significant decrease in the extent of mesopores adsorption. This is a clear indication of the efficiency of the impregnation route in dispersing the active phase within the mesoporous channels. Pore size distribution curves, calculated from the desorption branch (BJH method), confirm these findings, being the PSD centred at similar values for both the supports and the relative composites, although with a lower intensity for the latters. As expected, MCM41_M and MCM41_N show channels and wall thickness of about 2 nm, while SBA15, has pores of about 7 nm with thicker walls of about 4 nm (Table 1).

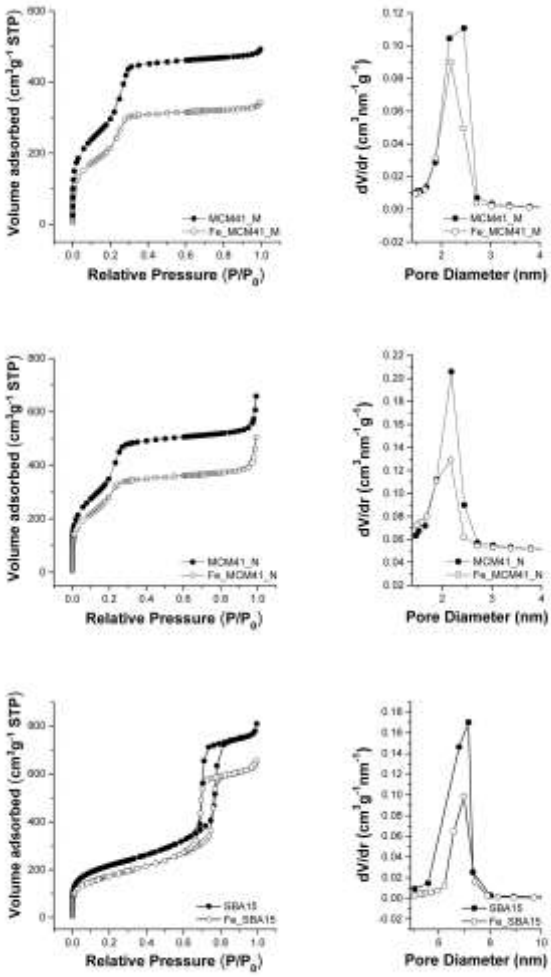

Fig. 3 N_2 adsorption-desorption isotherms and pore size distributions of the bare MCM-41 and SBA-15 and their corresponding iron oxide-based sorbents.

Sulphidation and regeneration processes

For each sorbent, three sulphidation cycles have been carried out in order to investigate the stability of the sorbent's performance (see Fig. S6†). B_t and SRC values of the micrometric (Fe_MCM41_M) and nanometric (Fe_MCM41_N) MCM-41-based sorbents are compared with the SBA-15-based

Please do not adjust margins

Please do not adjust margins

sorbent (Fe_SBA15) and a commercial unsupported ZnO sorbent (Katalco$_{JM}$ 32-5) (Table 2).

In the first sulphidation run, the Fe_MCM41_M micrometric sorbent shows the best sorption capacity (SRC = 38 mg$_S$ g$_{sorbent}^{-1}$), i.e. 1.5 times higher than that of nanometric Fe_ MCM41_N and 2.5 times higher than that of both Fe_SBA15 and the commercial Katalco$_{JM}$ 32-5 (Table 2). However, though preserving the highest SRC value, the Fe_MCM41_M sample shows a remarkable decrease (42%) in the sulphur retention capacity in the successive sulphidation processes. Such extent of reduction is significantly higher than that (26%) observed for the nanometric Fe_MCM41_N sorbent. By converse, the Fe_SBA15 sorbent does not show any difference of the SRC value between the first and the successive sulphidation runs (16 mg$_S$ g$_{sorbent}^{-1}$). However, it is worthy of note that the H_2S-removing performance of Fe_MCM41_M is always better than that of the SBA-15-based composite, since its SRC value after the first sulphidation step remains constant at 22 mg$_S$ g$_{sorbent}^{-1}$. The worst performance is exhibited by the commercial sorbent, whose SRC value, after the first sorption run, decreases to almost zero considering the experimental error.

The sulphidation process has been monitored by quadrupole mass spectrometry, which is proved to be an extremely useful technique, being able to follow the formation of the different gas species that can form during the different processes. The first sorption step of the most promising sorbent (Fe_MCMC41_M) is shown in Fig. 4a.

The removal of H_2S corresponds to the formation of a large amount of H_2O accompanied by a small amount of SO_2, according to the substitution reaction (equation 1) reported in the following. Fe_2S_3 is known to be a thermodynamically unstable phase that easily converts to pyrite[20] and Fe_3S_4[5,34] (equation 2) or pyrite, pyrrhotite and sulphur[35] (equation 3, where α, β, γ are the relative molar amounts). The formation of a small amount of SO_2 is justified by the redox reaction of H_2S which can lead to the formation of FeO (equation 4), as suggested by some authors;[36] as a consequence, a small amount of FeS can be formed (equation 5). Therefore, in the selected operating conditions, the sulphidation process is governed by the substitution reaction.

$$Fe_2O_3 + 3H_2S \rightarrow Fe_2S_3 + 3H_2O \quad (1)$$

$$2\,Fe_2S_3 \rightarrow FeS_2 + Fe_3S_4 \quad (2)$$

$$Fe_2S_3 \rightarrow \alpha\,FeS_2 + \beta FeS_x + \gamma S \quad (3)$$

$$3\,Fe_2O_3 + H_2S \rightarrow 6\,FeO + SO_2 + H_2O \quad (4)$$

$$FeO + H_2S \rightarrow FeS + H_2O \quad (5)$$

Unfortunately, due to the low content of the iron oxide active phase (10%w/w), and to the ultrasmall size of the particles (lower than the pore size), wide angle XRD analysis is not able to give incontrovertible information about the crystallographic phases formed during the sulphidation-regeneration processes (wide angle Fig. in S4†) and to confirm the proposed reaction scheme for H_2S removal.

The regeneration process of Fe_MCM41_M was carried out by heating the sample under flowing air (20 cm^3 g^{-1}) at 500 °C with a heating rate of 10 °C min^{-1}; the outlet gas composition was monitored by both a thermal conductivity detector (TCD) and a quadrupole mass spectrometer (QMS). The results are reported in Fig. 4b. The TCD profile is characterized by the presence of two main peaks: the first one, centred at about 210 °C, corresponding to the O_2 consumption (upper curve, QMS (O_2)), and the second one due to a slow SO_2 release at about 300 °C, as confirmed by the QMS (SO_2) bottom curve. A similar behaviour has been observed for Fe_SBA15, while, for the nanometric Fe_MCM41_N sorbent, a very slow gradual release of SO_2 is recorded up to 500 °C (Fig. S3†). This is in agreement with the possible reactions, expressed by equations 6,[37] 7[38] and 8, of the different iron sulphides with oxygen which lead to the regeneration of the iron oxide phase.

$$4FeS_2 + 11O_2 \rightarrow 2\,Fe_2O_3 + 8\,SO_2 \quad (6)$$

$$Fe_3S_4 + 2O_2 \rightarrow 2\,Fe_3O_4 + 4S \quad (7)$$

$$FeS_x + xO_2 \rightarrow Fe_2O_3 + xSO_2 \quad (8)$$

The reduced phase (FeS) could instead lead to the formation of sulphur:[39]

$$4\,FeS + 3O_2 \rightarrow 2\,Fe_2O_3 + \frac{1}{2}\,S_8 \quad (9)$$

In order to justify the decrease in the performance after the first H_2S-removing step, the possibility of a non-complete regeneration has been investigated by CHNS measurements.

The result evidences the presence of 1.4 wt% of sulphur in the regenerated sample and justifies the decrease in the SRC value as mainly due to the presence of residual iron sulphides. It cannot be excluded, however, that the active phase, when submitted to the regeneration process, undergoes changes in surface properties or crystallinity degree, as suggested in the literature.[20]

Table 2 Breakthrough time (Bt) and sulphur retention capacity (SRC) of fresh and regenerated iron oxide-based sorbents. R1 and R2 refer to the first regeneration and the second regeneration, respectively. The error in SRC value is estimated to be ± 2 mgS gsorbent-1.

Sample	Sulphidation run	B_t (s)	SRC (mg$_S$ g$_{sorbent}^{-1}$)
Fe_ MCM41_M	1st	295	38
Fe_ MCM41_M_R1	2nd	169	22
Fe_ MCM41_M_R2	3rd	169	22
Fe_ MCM41_N	1st	187	25
Fe_ MCM41_N_R1	2nd	163	18
Fe_ MCM41_N_R2	3rd	153	17
Fe_SBA15	1st	125	16
Fe_SBA15_R1	2nd	112	15
Fe_SBA15_R2	3rd	125	16
Katalco$_{JM}$ 32-5	1st	122	16
Katalco$_{JM}$ 32-5_R1	2nd	10	1
Katalco$_{JM}$ 32-5_R2	3rd	13	2

Please do not adjust margins

Please do not adjust margins

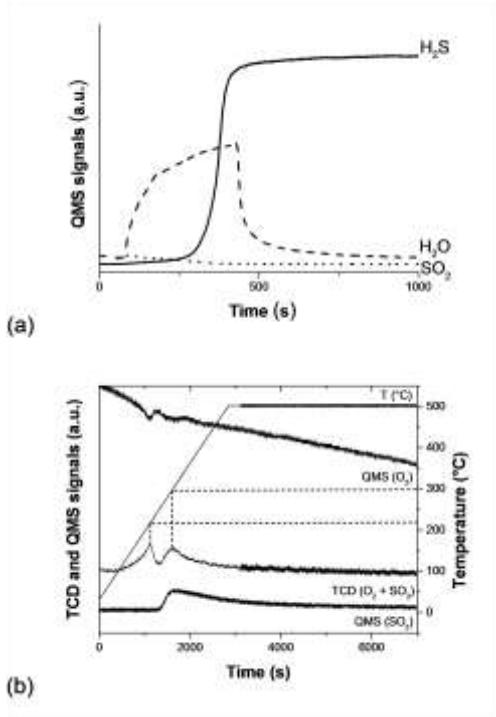

Fig. 4 (a) H_2S, SO_2 and H_2O breakthrough curves of the Fe_MCM41_M during the first sulphidation run and (b) TPD profile and SO_2 and O_2 Quadrupole Mass Spectrometer (QMS) signals of Fe_MCM41_M during the first regeneration run.

Regenerated sorbents characterization

In order to verify the stability after repeated sulphidation-regeneration cycles, N_2-physisorption and low angle XRD measurements have been performed on the MCM-41 composites after the third regeneration step (Fe_MCM41_M_R3 and Fe_MCM41_N_R3) and the results have been compared with those of the fresh sorbents (Fig. 5 and Table 3).

Low angle XRD analyses indicate that, despite the repeated sulphidation-regeneration cycles, the micrometric Fe_MCM41_M sample retains the hexagonal pore structure (Fig. 5a). Surface area, pore volume, and pore size distribution are also preserved, confirming the high stability of this sorbent. Conversely, a partial structural collapse as well as a worsening of the textural properties are observed for the nanometric sorbent (Fig. 5b), the latter ascribable to the decrease in both micro and mesopores contributions that lead to an almost completely microporous structure.

In order to better understand the actual reasons behind the behaviour of the nanometric sorbent, by considering that the sorbents have been tested three months later than their textural characterization, further measurements (low angle XRD and N_2-physisorption) have been repeated on a portion of the same sample not sulphided after three months aging (Fe_MCM41_N_aged).

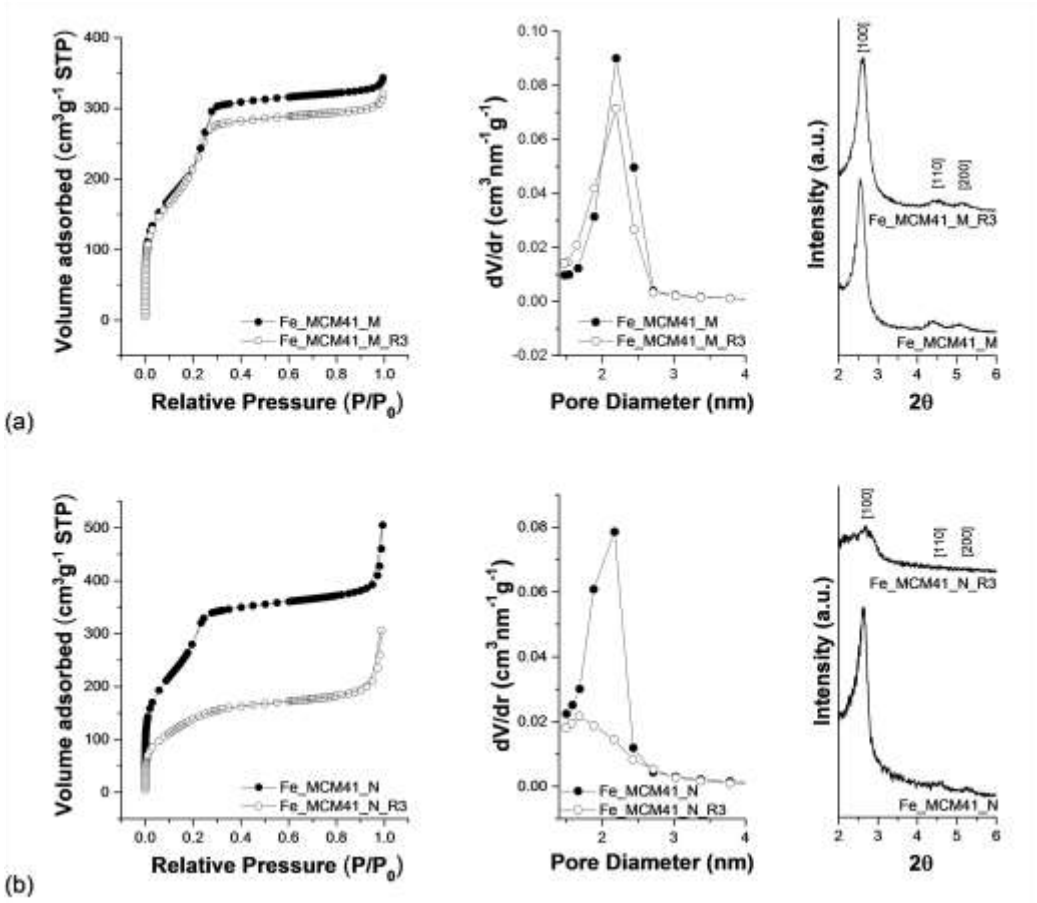

Fig. 5 N_2 adsorption-desorption isotherms, pore size distributions and Low angle XRD of: (a) Fe_MCM41_M and Fe_MCM41_M_R3; (b) Fe_MCM41_N and Fe_MCM41_N_R3.

This journal is © The Royal Society of Chemistry 20xx

Please do not adjust margins

Please do not adjust margins

Table 3 Textural features obtained by N_2-physisorption data for fresh and three times-regenerated composites. d-spacing (d_{100}) and lattice parameter (a_0) obtained from the X-Ray diffraction data.

Sample	S_{BET} (m^2g^{-1})	V_p (cm^3g^{-1})	D_{pore} (nm)	w_t (nm)	d_{100}	a_0
Fe_MCM41_M	768	0.53	2.2	1.6	3.47	4.0
Fe_MCM41_M_R3	771	0.49	2.2	1.7	3.41	3.9
Fe_MCM41_N	1007	0.58	2.2	1.7	3.33	3.9
Fe_MCM41_N_aged	651	0.37	1.7	2.2	3.28	3.8
Fe_MCM41_N_R3	496	0.29	1.7	2.0	3.26	3.7

The comparison between the textural properties of the fresh (as-prepared Fe_MCM41_N) and aged (Fe_MCM41_N_aged) nanometric sorbents (Fig. S2†) pointed out that, during the aging time, the water present in the air can react with the silica surface by hydrolyzing the Si-O-Si bonds and forming silanols groups. This induces the reorganization of the porous structure with the consequent loss of mesoporosity.[40]

Discussion

The obtained results highlight that the use of MCM-41, as an alternative support to the most common SBA-15 and other porous amorphous alumina and silica, leads to efficient and highly regenerable sorbents for H_2S removal at mid-temperature. Furthermore, being the composite regenerable at temperatures even lower than the temperature of the sulphidation process (300 °C), the iron oxide active phase proves to be promising for the development of a new generation of solid sorbents for processes based on IGCC systems, also due to its low cost and low-toxicity.[21] MCM-41 is rarely used in applications at mid- and high-temperature[41,42] probably because of the possible collapse of the mesoporous structure, "theoretically fragile" owing to its small pore size and small wall thickness. This work clearly shows that, at the same conditions, in terms of sulphidation (300 °C) and regeneration (500 °C) temperatures, MCM41_M-based sorbents retain their stability as the most robust counterpart based on micrometric SBA-15. The porous structure stability of the support might be correlated to the size of the particles, since the micrometric Fe_MCM41_M sorbent retains its porous structure also after the third regeneration at 500 °C in air, which is not the case of the nanometric Fe_MCM41_N samples (Table 3).

In order to study the effect of the pore size and the corresponding surface area, a comparison of the SRC values between the two micrometric sorbents (Fe_MCM41_M and Fe_SBA15) (Fig. 6a) with the same hexagonal porous (*p6mm*) structure and iron oxide content (10% w/w) is carried out. The results highlight that the surface area seems to be the key factor for improving the performance. In fact, being the kinetic diameter of H_2S and N_2 very similar,[43] the surface area calculated by N_2-physisorption should be considered as the effective surface accessible to H_2S molecules.[44] Going from micrometric SBA-15 to micrometric MCM-41 an increase of 28%-30% in the surface area has been observed for both the bare supports (SBA15 MCM41_M, see Table 1) and the corresponding composites (Fe_SBA15 and Fe_MCM41_M). As a consequence, the SRC value for Fe_MCM41_M is always higher than that for Fe_SBA15, and from the second sulphidation step it stabilizes at a value 35% higher than that of Fe_SBA15. These findings are in contrast with those obtained by other authors[45] for ZnO-based sorbents, who found a better performance for the SBA-15-based sorbents than for the MCM-41 ones. This result could be justified by considering both the different impregnation strategy and the different active phase, as well as its dispersion in the mesochannels. In fact, it is reported in the literature that zinc cations have a high affinity for silanol groups; this strong interaction induces the formation of a thin layer of amorphous zinc oxide phase,[17,20,46] while small iron oxide nanoparticles are instead formed from iron (III) salts using the same impregnation strategy.[20]

In order to study the effect of the accessibility of the active phase, a further comparison of the SRC values is attempted using micrometric and nanometric MCM-41 based sorbents (Fig. 6b). In the case of the MCM41_N support, nanoparticles have been obtained by using ethyl acetate as growth inhibitor during the synthesis. Reducing the particle size down to the nanoscale induces a reduction in the pore length, thus facilitating, at least in principle, the H_2S accessibility to the iron oxide active phase. Furthermore, the synthesized nanometric composite (Fe_MCM41_N) showed a surface area (1007 $m^2 g^{-1}$) 30% higher than that of the micrometric MCM-41 composite (768 $m^2 g^{-1}$). By considering the key role of the surface area and the reduced length of the pores, nanometric systems would be ideal sorbents for improving the sulphur retention capacity. However, in all sulphidation steps, the nanometric sorbent showed a worst performance when compared to the micrometric one (Fig. 6b). The actual reason can be understood by comparing the N_2-isotherms and the low angle XRD data recorded soon after its preparation (as-prepared), after three months of aging (aged) and after the third regeneration process (R3) (see Fig. 5). The decrease in surface area from 1007 $m^2 g^{-1}$ to 651 $m^2 g^{-1}$ (35% of reduction) can be ascribed to the possible closing of the pores due to the reaction with water present in the air after three months of aging.

Please do not adjust margins

Please do not adjust margins

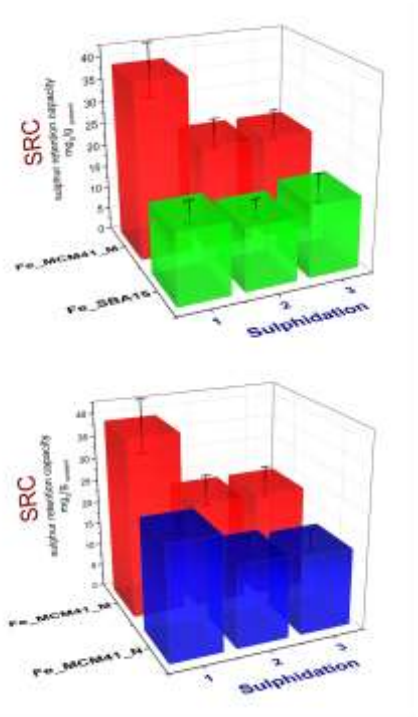

Fig. 6 Comparison of SRC values of (a) micrometric sorbents: FeSBA15 versus FeMCM41_M and (b) micrometric and nanometric MCM41 Fe_MCM41_M and Fe_ MCM41_N sorbents.

This is confirmed also by other studies reported in the literature, in which it has been demonstrated that nanoparticles of MCM-41 undergo evident changes in their porous structure both when they are in contact with air[47] or are dispersed in water.[48,49] A further decrease down to 496 m^2 g^{-1} is caused by the repeated sulphidation-regeneration cycles, probably because of the presence of water formed in the reaction between iron oxide and H_2S during the sulphidation process (equation 1). These findings demonstrate that, besides the optimization of the surface area, an important factor to be taken into account to design an efficient and regenerable sorbent is the stability of the support porous structure, which is strictly related to the accessibility of the active phase. Although the micrometric and nanometric MCM-41 sorbents are characterized by the same pore size distribution and wall thickness, when the particle sizes are reduced down to the nanometer scale, surface effects prevail, thus compromising the sorbent performances. However, it should be underlined that the nanometric sorbent (Fe_MCM41_N) shows a better stability during the sulphidation-regeneration cycles, a decrease of about 28% in the SRC value being observed between the first and the second sulphidation step, remarkable lower than that showed by the micrometric sorbent (42%).

Conclusions

Mesostructured Fe_2O_3@MCM-41 composites have been proved to be promising sorbents for H_2S removal at mid-temperature due to the high surface area and the homogenous dispersion of ultrasmall particles of maghemite within the small mesopores. The comparison with an analogous silica-based sorbent (Fe_SBA15) and with a commercial sorbent highlights their superior performance, with a sulphur retention capacity that reaches the highest value for the micrometric MCM41-based sorbent (38 mg_S $g_{sorbent}^{-1}$, compared to 25 mg_S $g_{sorbent}^{-1}$ and 16 mg_S $g_{sorbent}^{-1}$ for the Fe_MCM41_N and Fe_SBA15 composites, respectively). The optimization of the surface area by reducing the pore size and wall thickness with respect to SBA15 was found to be a remarkable aspect for the improvement of the sulphur retention capacity. However, the comparison of the efficiency of the micrometric and nanometric MCM41-based sorbents in removing H_2S evidenced that other factors, as the stability of the porous structure during their storing and use, must be taken into account. The repeated sulphidation-regeneration cycles showed that, after a first decrease in the SRC value between the first and the second sulphidation steps, the H_2S sorption capacity of the Fe_2O_3@MCM-41 composites is preserved, suggesting their potential application as sorbents in mid-temperature processes. The proposal of this class of materials as alternative sorbents for highly efficient IGCC plants is also supported by the results of their regeneration, which was observed to occur at about 300 °C, temperature at which the sulphidation step is performed. Furthermore, the synthetic strategy of the composites is simple, reproducible, and does not involve purification steps, thus allowing it to be easily scaled-up.

Acknowledgements

Consorzio AUSI (Consorzio per la promozione delle Attivita Universitarie del Sulcis-Iglesiente) is gratefully acknowledged for the grant financing for C. Cara and A. Ardu. P.O.R. Sardegna F.S.E. is acknowledged for the grant financing of M Sanna Angotzi. The use of the HRTEM facilities of C.G.S. (Centro Grandi Strumenti, University of Cagliari) is gratefully acknowledged. This research used resources of the Center for Functional Nanomaterials, which is a U.S. DOE Office of Science Facility, at Brookhaven National Laboratory under Contract No. DE-SC0012704.

References

1 M. D. Dolan, A. Y. Ilyushechkin, K. G. McLennan and S. D. Sharma, *Asia-Pacific J. Chem. Eng.*, 2012, **7**, 1–13.

2 S. Cheah, D. L. Carpenter and K. A. Magrini-Bair, *Energy and Fuels*, 2009, **23**, 5291–5307.

3 A. Samokhvalov and B. J. Tatarchuk, *Phys. Chem. Chem. Phys.*, 2011, **13**, 3197–209.

4 P. R. Westmoreland and D. P. Harrison, *Environ. Sci.*, 1976, **10**, 659–661.

5 A. Davydov, K. T. K. K. T. Chuang and A. A. R. Sanger, *J. Phys. Chem. B*, 1998, **102**, 4745–4752.

6 J. M. Sánchez-Hervás, J. Otero and E. Ruiz, *Chem. Eng. Sci.*, 2005, **60**, 2977–2989.

This journal is © The Royal Society of Chemistry 20xx

Please do not adjust margins

Please do not adjust margins

7 R. Turton, D. A. Berry, T. H. Gardner and A. Miltz, *Ind. Eng. Chem. Res.*, 2004, **43**, 1235–1243.

8 P. V Ranade and D. P. Harrison, *Chem. Eng. Sci.*, 1981, **36**, 1079–1089.

9 R. Portela, F. Rubio-Marcos, P. Leret, J. F. Fernández, M. a. Bañares and P. Ávila, *J. Mater. Chem. A*, 2014, **3**, 1306–1316.

10 S. Varghese, M. G. Cutrufello, E. Rombi, C. Cannas, R. Monaci and I. Ferino, *Appl. Catal. A Gen.*, 2012, **443–444**, 161–170.

11 E. Rombi, M. G. Cutrufello, C. Cannas, M. Casu, D. Gazzoli, M. Occhiuzzi, R. Monaci and I. Ferino, *Phys. Chem. Chem. Phys.*, 2009, **11**, 593–602.

12 R. Huirache-Acuña, R. Nava, C. Peza-Ledesma, J. Lara-Romero, G. Alonso-Núez, B. Pawelec and E. Rivera-Muñoz, *Materials (Basel).*, 2013, **6**, 4139–4167.

13 H. F. Garces, H. M. Galindo, L. J. Garces, J. Hunt, A. Morey and S. L. Suib, *Microporous Mesoporous Mater.*, 2010, **127**, 190–197.

14 C. Cannas, A. Ardu, A. Musinu, L. Suber, G. Ciasca, H. Amenitsch and G. Campi, *ACS Nano*, 2015, **9**, 7277–7286.

15 C. Cannas, A. Ardu, D. Peddis, C. Sangregorio, G. Piccaluga and A. Musinu, *J. Colloid Interface Sci.*, 2010, **343**, 415–422.

16 C. Cannas, A. Ardu, A. Musinu, D. Peddis and G. Piccaluga, *Chem. Mater.*, 2008, **20**, 6364–6371.

17 M. Mureddu, I. Ferino, E. Rombi, M. G. Cutrufello, P. Deiana, A. Ardu, A. Musinu, G. Piccaluga and C. Cannas, *Fuel*, 2012, **102**, 691–700.

18 B. Elyassi, Y. Al Wahedi, N. Rajabbeigi, P. Kumar, J. S. Jeong, X. Zhang, P. Kumar, V. V. Balasubramanian, M. S. Katsiotis, K. Andre Mkhoyan, N. Boukos, S. Al Hashimi and M. Tsapatsis, *Microporous Mesoporous Mater.*, 2014, **190**, 152–155.

19 A. S. Araújo, M. J. B. Souza, A. O. S. Silva, A. M. G. Pedrosa, J. M. F. B. Aquino and A. C. S. L. S. Coutinho, *Adsorption*, 2005, **11**, 181–186.

20 M. Mureddu, I. Ferino, A. Musinu, A. Ardu, E. Rombi, M. G. Cutrufello, P. Deiana, M. Fantauzzi and C. Cannas, *J. Mater. Chem. A*, 2014, **2**, 19396–19406.

21 A. Hervault and N. T. K. Thanh, *Nanoscale*, 2014, **6**, 11553–11573.

22 D. Zhao, J. Feng, Q. Huo, M. Nicholas, G. H. Fredrickson, B. F. Chmelka and G. D. Stucky, *Science (80-.).*, 1998, **279**, 548–552.

23 J. S. Beck, J. C. Vartuli, W. J. Roth, M. E. Leonowicz, C. T. Kresge, K. D. Schmitt, C. T.-W. Chu, D. H. Olson, E. W. Sheppard, S. B. McCullen, J. B. Higgins and J. L. Schlenkert, *J. Am. Chem. Soc.*, 1992, 10834–10843.

24 J. Haber, J. H. Block and B. Delmon, *Pure Appl. Chem.*, 1995, **67**, 1257–1306.

25 E. Murad and J. H. Johnston, in *Mössbauer Spectroscopy Applied to Inorganic Chemistry*, ed. G. Long, Plenum Publ. Corp., New York, 1987, pp. 507–583.

26 R. Cornell and U. Schwertmann, *The Iron Oxides*, 2003.

27 C. Cara, A. Musinu, V. Mameli, A. Ardu, D. Niznansky, J. Bursik, M. A. Scorciapino, G. Manzo and C. Cannas, *Cryst. Growth Des.*, 2015, **15**, 2364–2372.

28 L. A. Mercante, W. W. M. Melo, M. Granada, H. E. Troiani, W. A. A. Macedo, J. D. Ardison, M. G. F. Vaz and M. A. Novak, *J. Magn. Magn. Mater.*, 2012, **324**, 3029–3033.

29 O. Moscoso-Londoño, M. S. Carrião, C. Cosio-Castañeda, V. Bilovol, R. M. Sánchez, E. J. Lede, L. M. Socolovsky and R. Martínez-García, *Mater. Res. Bull.*, 2013, **48**, 3474–3478.

30 L. J. Allen, A. J. D'Alfonso, B. Freitag and D. O. Klenov, *MRS Bull.*, 2012, **37**, 47–52.

31 P. Schlossmacher, D. O. Klenov, B. Freitag, S. Von Harrach and A. Steinbach, *Microsc. Anal. Nanotechnol. Suppl.*, 2010, **24**, S5–S8.

32 M. Thommes, K. Kaneko, A. V. Neimark, J. P. Olivier, F. Rodriguez-Reinoso, J. Rouquerol and K. S. W. Sing, *Pure Appl. Chem.*, 2015, **87**, 1051–1069.

33 M.-H. Kim, H. Na, Y. Kim, S. Ryoo, H. S. Cho, K. E. Lee, H. Jeon, R. Ryoo and D.-H. Min, *ACS Nano*, 2011, **5**, 3568–3576.

34 G. Huang, E. He, Z. Wang, H. Fan, J. Shangguan, E. Croiset and Z. Chen, *Ind. Eng. Chem. Res.*, 2015, **54**, 8469–8478.

35 P. G. Stansberry, J. P. Wann, W. R. Stewart, J. Yang, J. W. Zondlo, A. H. Stiller and D. B. Dadyburjor, *Fuel*, 1993, **72**, 793–796.

36 Y. H. Lin, Y. C. Chen and H. Chu, *Chemosphere*, 2015, **121**, 62–67.

37 R. Walker, A. D. Steele and T. D. B. Morgan, *Surf. Coatings Technol.*, 1988, **34**, 163–175.

38 S. Boursiquol, M. Mullet, M. Abdelmoula, J. M. Génin and J. J. Ehrhardt, *Phys. Chem. Miner.*, 2001, **28**, 600–611.

39 K. J. Cantrell, S. B. Yabusaki, M. H. Engelhard, A. V. Mitroshkov and E. C. Thornton, *Environ. Sci. Technol.*, 2003, **37**, 2192–2199.

40 J. Yu, J.-L. Shi, L.-Z. Wang, M.-L. Ruan and D.-S. Yan, *Mater. Lett.*, 2001, **48**, 112–116.

41 C. Wu, Y. Kong, F. Gao, Y. Wu, Y. Lu, J. Wang and L. Dong, *Microporous Mesoporous Mater.*, 2008, **113**, 163–170.

42 G. K. Chuah, X. Hu, P. Zhan and S. Jaenicke, *J. Mol. Catal. A Chem.*, 2002, **181**, 25–31.

43 D. W. Breck, *Zeolite Molecular Sieves: Structure, Chemistry and Use*, New York, John Wiley., 1974.

44 M. Jahandar Lashaki, M. Fayaz, S. Niknaddaf and Z. Hashisho, *J. Hazard. Mater.*, 2012, **241–242**, 154–163.

45 M. Hussain, N. Abbas, D. Fino and N. Russo, *Chem. Eng. J.*, 2012, **188**, 222–232.

46 C. Cannas, M. Casu, A. Lai, A. Musinu and G. Piccaluga, *J. Mater. Chem.*, 1999, 1765–1769.

47 L. Y. Chen, S. Jaenicke and G. K. Chuah, *Microporous Mater.*, 1997, **12**, 323–330.

48 C. M. Carbonaro, F. Orrù, P. C. Ricci, A. Ardu, R. Corpino, D. Chiriu, F. Angius, A. Mura and C. Cannas, *Microporous Mesoporous Mater.*, 2016, **225**, 432–439.

49 J. Trébosc, J. W. Wiench, S. Huh, V. S.-Y. Lin and M. Pruski, *J. Am. Chem. Soc.*, 2005, **127**, 3057–3068.

Please do not adjust margins